

# A Calibration System for Compton Polarimetry at $e^+e^-$ Linear Colliders

Benedikt Vormwald<sup>1,2</sup>, Jenny List<sup>1</sup>, and Annika Vauth<sup>1,2</sup>

1- Deutsches Elektronen-Synchrotron DESY  
Notkestr. 85, 22607 Hamburg, Germany

2- Universität Hamburg, Institut für Experimentalphysik  
Luruper Chaussee 149, 22761 Hamburg, Germany

## Abstract

Polarimetry with permille-level precision is essential for future electron-positron linear colliders. Compton polarimeters can reach negligible statistical uncertainties within seconds of measurement time. The dominating systematic uncertainties originate from the response and alignment of the detector which records the Compton scattered electrons. The robust baseline technology for the Compton polarimeters foreseen at future linear colliders is based on an array of gas Cherenkov detectors read out by photomultipliers. In this paper, we will present a calibration method which promises to monitor nonlinearities in the response of such a detector at the level of a few permille. This method has been implemented in an LED-based calibration system which matches the existing prototype detector. The performance of this calibration system is sufficient to control the corresponding contribution to the total uncertainty on the extracted polarisation to better than 0.1%.

# 1 Introduction

Since the event rates of electroweak processes depend on the chirality of the colliding particles, beam polarisation is a key ingredient of the physics programme of future electron-positron colliders [1] and its precise knowledge is as important as the knowledge of the luminosity. Thereby, the luminosity-weighted average polarisations at the interaction point  $\langle \mathcal{P} \rangle_{\text{lumi}}$ , which is the value relevant for the interpretation of collider data, have to be determined by combining fast measurements of Compton polarimeters with long-term scale calibration obtained from reference processes in collision data.

In particular for the International Linear Collider [2], where both beams are foreseen to be longitudinally polarised, it is required to control  $\langle \mathcal{P} \rangle_{\text{lumi}}$  with per mille-level precision in order not to limit the precision of cross-section measurements. Two Compton polarimeters [3] per beam aim to measure the longitudinal polarisation before and after the collision with a precision of  $\delta \mathcal{P} / \mathcal{P} \leq 0.25\%$ <sup>1</sup>. It should be noted, though, that this goal is not driven by physics requirements, but by what used to be considered feasible experimentally. Thus, further improvements in polarimetry would still have direct benefits for the physics potential of the machine.

In order to evaluate the effects on the mean polarisation vector caused by the beamline magnets between the polarimeters and the interaction point, by the detector magnets and by the beam-beam interaction, spin tracking simulations are required. These effects have recently been studied in [4], concluding that not only a cross-calibration of the polarimeters to 0.1% is feasible, but also individual extrapolations of upstream and downstream measurements to the  $e^+e^-$  interaction point.

From reference  $e^+e^-$  reactions, the long-term average of the polarisation at the interaction point can be determined. In particular  $W$  pair production [5–7] and single  $W$  production [8] have been studied in this respect, showing that precisions of about 0.15% can be achieved after several years of data taking. These results are quite robust with regard to systematic uncertainties: e.g. in the measurement using  $W$  pair production, even for a conservative assumption of 0.5% uncertainty on the selection efficiency for the signal and 5% for the background, the impact on the uncertainty of the polarisation measurement was found to be below the statistical uncertainty for an integrated luminosity of  $500 \text{ fb}^{-1}$  [6]. Any imperfection in the beam helicity reversal, i.e. differences in the magnitude of the polarisation between measurements with left- and right-handed polarised beams, has to be corrected for based on the polarimeter measurements.

The two polarimeters per beam are located about 1.8 km upstream and 160 m downstream of the interaction point, providing non-destructive measurements of the longitudinal beam polarisation based on the polarisation dependence of Compton scattering. They have been designed for operation at beam energies between 45 GeV and 500 GeV. Several options for detecting the Compton-scattered electrons<sup>2</sup> are being considered. The baseline solution is a gas Cherenkov detector consisting of 20 channels, each 1 cm wide. A two-channel prototype of such a detector has been successfully operated in testbeam, where the alignment

---

<sup>1</sup>for typical ILC beam polarisation values of  $\mathcal{P}_{e^-} \geq 80\%$  and  $\mathcal{P}_{e^+} \geq 30\%$  or even  $\geq 60\%$ .

<sup>2</sup>or positrons in case of the positron beam of the ILC which is equipped analogously. Throughout this paper, we'll use "electron" to refer to both cases, unless explicitly stated otherwise.

requirement for the ILC has nearly been reached and electronic noise was found to be at a negligible level [9]. The remaining challenge for per mille-level polarimetry with a gas Cherenkov detector is the linearity of the device.

In this paper, we present a calibration system which is able to monitor nonlinearities with sufficient precision and provides the abilities to correct for them. The paper is organised in three main parts: In section 2, we summarise the most important facts about the ILC Compton polarimeters before introducing the baseline detector for the Compton scattered electrons and discussing the systematic uncertainties of the measurement, which define the target precision of the calibration system. In section 3, we introduce a suitable linearisation method, discuss the resulting requirements, and present a realisation of a suitable light source. The performance of the calibration system and its application to the ILC Compton polarimeters will be discussed in section 4 before concluding in section 5.

## 2 Compton Polarimetry at the ILC

Compton scattering of circularly polarised laser light off the lepton beam is the method of choice for polarimetry at high-energy colliders for a number of reasons: As a pure QED process, the scattering cross-section can be calculated precisely, with radiative corrections less than 0.1% [10], and offers large polarisation asymmetries. The interaction with the laser conserves the beam quality so that polarimetry does not interfere with collision data taking. The laser polarisation can be flipped very quickly using e.g. a Pockel's cell and its absolute value can be controlled at the level of 0.1% [11]. Backgrounds will be determined in-situ by shutting the laser off and thus can easily be corrected for.

Compton polarimetry was successfully employed at many previous accelerators, for instance at the SLC [11] or at HERA [12, 13]. In this section, we will summarise the most important generic aspects of Compton polarimetry following the notation from [14], before summarising the current design of the polarimeters foreseen at the ILC. Additional details on the ILC polarimeters can be found in [3].

### 2.1 Compton Polarimetry Basics

The kinematics of Compton scattering are fully determined by two variables, e.g. the azimuthal and polar angle of the scattered electron. In particular, the polar angle is equivalent to the energy of the scattered electron. Besides the unpolarised part, the double-differential Compton cross section [15] contains terms proportional to the linear light polarisation and to the product of circular light polarisation and transverse or longitudinal electron polarisation. When integrating the cross section over the full azimuthal angle, only the term containing the longitudinal polarisation remains, so that any sensitivity to linear light polarisation and transverse electron polarisation is removed. Thus transverse beam polarisation requires a double differential measurement in energy and e.g. vertical position<sup>3</sup>, while for longitudinal polarimetry, which is the primary concern

---

<sup>3</sup>For a recent discussion of transverse polarimetry at the ILC c.f. [16].

at the ILC, it is sufficient to measure either the energy of the scattered electron or the scattered photon.

The minimum energy of the electrons is given by the Compton edge energy

$$E_{\min} = E_0 \frac{1}{1+x} \quad , \quad (1)$$

where  $E_0$  is the beam energy, while the dimensionless variable  $x$  relates  $E_0$  to the energy of the laser photons  $\omega_0$ , the electron mass  $m$  and the crossing angle  $\theta_0$  between the electron beam and the laser:

$$x = \frac{4E_0\omega_0}{m^2} \cos^2(\theta_0/2) \simeq \frac{4E_0\omega_0}{m^2} \quad (2)$$

For e.g. a green laser ( $\omega_0 = 2.33$  eV) shining head-on to an electron beam with  $E_0 = 250$  GeV,  $x \simeq 9$  and thus  $E_{\min} \simeq 0.1E_0 = 25$  GeV, whereas the remaining energy is carried away by the photon.

In the laboratory frame, both the scattered electrons and photons are contained in a narrow forward cone around the electron beam direction, with typical opening angles of  $10 - 20 \mu\text{rad}$ .

The differential Compton scattering cross section with respect to the normalised photon energy  $y = \omega/E_0$  can be written as [15]

$$\frac{d\sigma(\lambda, \mathcal{P}_z)}{dy} = \frac{2\sigma_0}{x} \left[ \frac{1}{1-y} + 1 - y - 4r(1-r) + \mathcal{P}_z \lambda r x (1-2r)(2-y) \right] \quad (3)$$

or with respect to the absolute energy of the Compton scattered electron it becomes

$$\frac{d\sigma}{dE} = \frac{1}{E_0} \frac{d\sigma}{dy}, \quad (4)$$

where

$$\sigma_0 = 249.5 \text{ mb} \quad \text{and} \quad r = \frac{y}{x(1-y)}. \quad (5)$$

$\mathcal{P}_z$  is the longitudinal electron beam polarisation and  $\lambda$  describes the laser polarisation. Thus, the differential cross section is separated into a spin-independent and spin-dependent part. For convenience of the reader we note that  $r = 1$  corresponds to the Compton edge.

From equation 3 it can be seen that the asymmetry between the differential cross sections corresponding to the two laser helicity states  $\text{sgn } \lambda = \pm 1$  is proportional to the product of laser and beam polarisation:

$$\mathcal{A}(\mathcal{P}_z) = \frac{d\sigma^-(\mathcal{P}_z) - d\sigma^+(\mathcal{P}_z)}{d\sigma^-(\mathcal{P}_z) + d\sigma^+(\mathcal{P}_z)} \propto |\lambda \mathcal{P}_z| \quad (6)$$

Herein,  $\sigma^+$  ( $\sigma^-$ ) denotes the case of parallel (anti-parallel) laser and electron helicities. The proportionality factor is given by the inverse of the analysing power  $\mathcal{AP}$ , which is the asymmetry expected for  $\lambda \mathcal{P}_z = 100\%$ .

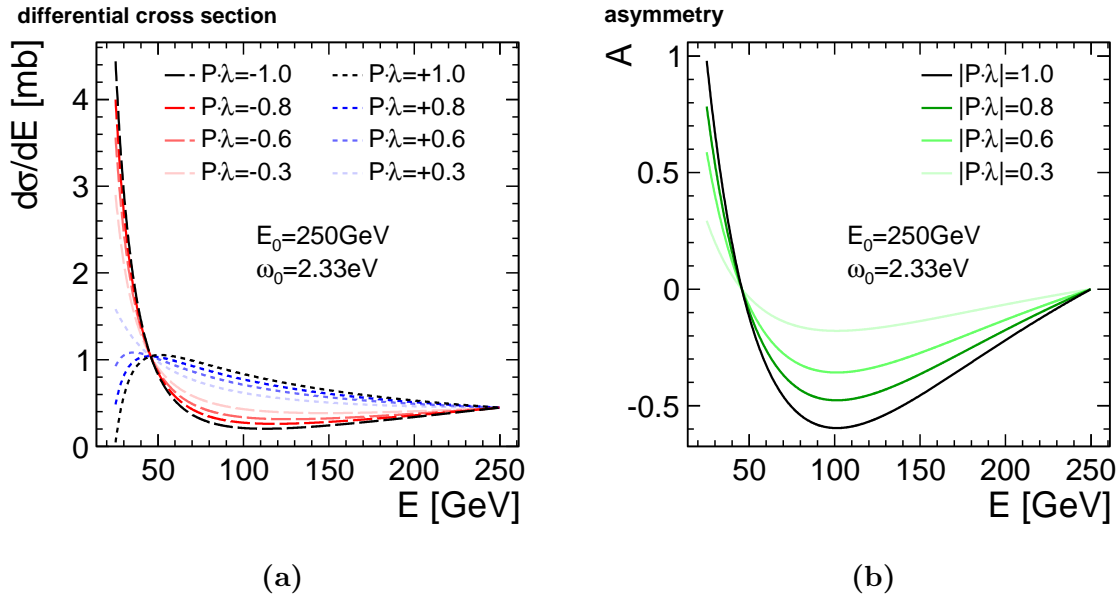


**Figure 1:** (a) Differential Compton scattering cross section for a beam energy of  $E_0 = 250$  GeV and green laser light. The different colours show the dependence of the differential cross section on the product of laser and beam polarisation. (b) Asymmetry for different absolute values of the beam polarisation. The asymmetry corresponding to  $|\mathcal{P}_z \cdot \lambda| = 1.0$  (black) is also called analysing power.

Figure 1 shows the differential Compton scattering cross section as well as the corresponding asymmetry for different beam polarisations with respect to the energy of the Compton scattered electron. In these figures, the beam energy is set to  $E_0 = 250$  GeV and a green laser is chosen, as this reflects the ILC baseline design parameters.

In practice,  $d\sigma$  will be determined by measuring the count rate in a detector channel with finite size, typically after converting the energy spectrum of the Compton scattered electrons into a position distribution via a magnetic chicane, as will be explained in the next section. Per channel  $i$ , the observed asymmetry is given by

$$\mathcal{A}_i = \frac{N_i^-(\mathcal{P}_z) - N_i^+(\mathcal{P}_z)}{N_i^-(\mathcal{P}_z) + N_i^+(\mathcal{P}_z)} \propto \mathcal{P}_z, \quad (7)$$

assuming the same luminosities for both laser helicities.

The measured polarisation values from the individual channels can then be combined into a weighted average, where the weights  $w_i$  are chosen to minimise the total statistical uncertainty, which is achieved by giving the largest weights to the channels with largest analysing power  $\mathcal{AP}_i$  [14]:

$$w_i = \frac{1}{(\mathcal{P}_z \cdot \mathcal{AP}_i)^{-2} - 1} \quad (8)$$

## 2.2 The ILC Compton Polarimeters

The ILC Compton polarimeters will be operated in a multi-event mode with  $\mathcal{O}(10^3)$  Compton interactions per bunch crossing. For the polarisation measurement, both the scattered photon and electron can be analysed equivalently. At HERA, the longitudinal polarimeter operated successfully in a multi-photon mode by detecting the sum of the photon energies in a calorimeter [17]. At ILC energies and intensities, however, the cumulative energy of  $\mathcal{O}(10^3)$  photons carrying on average  $\mathcal{O}(10)$  GeV each would amount to  $\mathcal{O}(10)$  TeV per bunch crossing, all within a narrow cone of  $\mathcal{O}(10)$   $\mu\text{rad}$ . Therefore, it seems highly unlikely that photon detection could contribute to precision polarimetry at the ILC.

The situation is very different for the detection of the scattered electrons as employed at SLD. As charged particles, the electrons can be energy-analysed by dipole magnets. This translates the energy measurement into a position measurement which does not require a total absorption of the energy. Thus, the shape of the spectrum can be monitored under multi-event conditions. Additionally, regions of high or low analysing power can be evaluated separately and enter in the total measurement with an appropriate weight (c.f. equation 8).

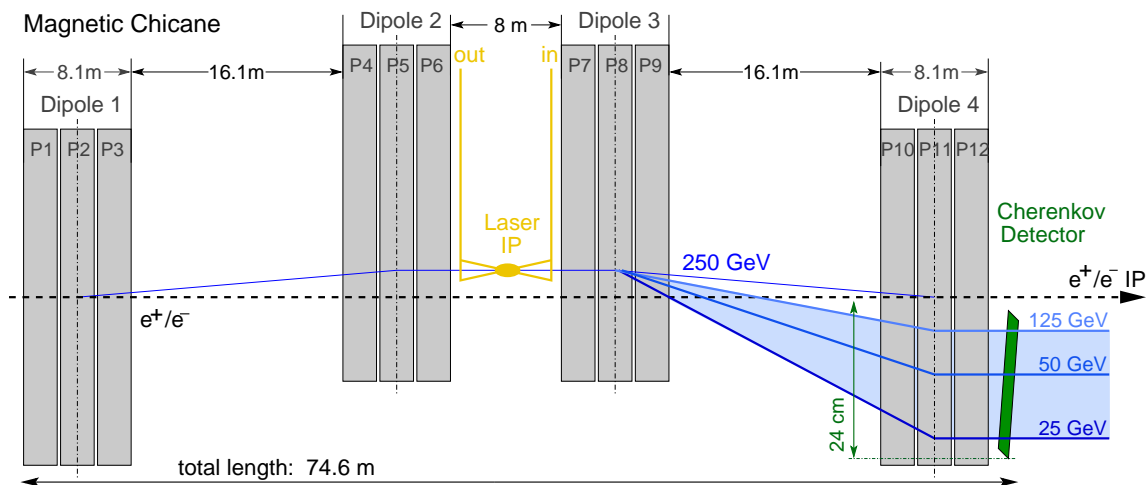


**Figure 2:** Sketch of the magnetic spectrometer for the ILC upstream polarimeter (from [9]). The Compton-scattered electrons with the lowest energies are deflected most by the spectrometer.

The polarimeter chicanes consist of a sets of dipole magnets. Figure 2 shows as an example a sketch of the chicane foreseen for the ILC's upstream polarimeters. The magnetic field strengths of the magnets are chosen such that the fan of Compton scattered electrons are deflected far enough from the main beam so that a segmented counting detector can be safely placed and operated next to the beam pipe. Both the upstream and the downstream polarimeter chicanes will be operated at a constant magnetic field for all beam energies. This implies that the Compton interaction point moves laterally with the beam energy, but offers the advantage that the position and size of the Compton spectrum in the detection plane stays invariant. Thus, the same measurement quality can be maintained

for all beam energies. A detailed description of the polarimeter chicane designs for the up- and downstream polarimeter is discussed in reference [3].

### 2.2.1 The Upstream Polarimeters at the ILC

At the upstream polarimeter, the beam spot of the yet undisturbed bunches is small and low background levels are expected [14]. Therefore, conventional lasers featuring moderate pulse energies can be used in order to probe every single bunch in an ILC bunch train. Different ILC beam parameter sets foresee between 1312 and 2625 bunches per bunch train, where the trains last 1 ms each and occur with a repetition rate of 5 Hz [2]. The ability to probe every bunch in a bunch train allows to accumulate high statistics in a very short time. Furthermore, it allows to resolve possible variations in the bunch polarisation within a bunch train which could be present due to beam dynamics.

On the downside, the expected radiation exposure of the detector from the Compton electrons alone amounts to up to about 1 MGy per year, which requires to employ sufficiently radiation hard detector technologies. The resulting readout rate in the order of 10 MHz requires a fast responding detector as well as fast readout electronics.

The upstream polarimeter chicane as sketched in figure 2 spreads the Compton spectrum over approx. 20 cm in the horizontal plane. Due to the benign conditions, the instrumentation can cover nearly the whole spectrum down to about 2 cm from the undisturbed main beam, corresponding to Compton electrons up to  $E = 125$  GeV. This clearly includes the zero crossing point of the asymmetry (c.f. figure 1b), which together with the Compton edge position provides important calibration reference.

### 2.2.2 The Downstream Polarimeters at the ILC

The downstream polarimeter chicane starts 120 m behind the  $e^+e^-$  interaction point, where the Compton interaction point is located at a secondary focus point of the machine optics. However, due to the energy loss during collisions, the beam cross section is four orders of magnitudes larger than at the upstream polarimeter [4]. In addition, significant beam background at the level of  $\mathcal{O}(10^3)$  photons and  $\mathcal{O}(10^2)$  charged particles per bunch crossing is expected [18]. For this reason, the laser power needs to be increased by more than three orders of magnitude to still maintain a reasonable signal to background ratio. This, in turn, reduces the maximal laser repetition rate to  $\mathcal{O}(1)$  laser pulse per ILC bunch train. Therefore, the detector readout speed is of no concern.

For the same reason, the radiation dose due to the Compton electrons themselves is three orders of magnitude lower than at the upstream polarimeter. On the other hand, the substantial backgrounds, which are present for every bunch independently of the presence of a laser pulse, will add to the total radiation dose. Thus it seems prudent to keep similar radiation tolerance requirements as for the upstream polarimeter.

Since the extraction line is designed with an aperture of 0.75 mrad with respect to the interaction point, the polarimeter detector needs to be placed in a distance of 15 cm to

the main beam trajectory. In order to still be able to probe a significant part of the fan of Compton scattered electrons, the polarimeter chicane is slightly modified and two additional magnets operating at a higher field strength are inserted in the spectrometer part resulting in a larger dispersion [19]. At a beam energy of  $E = 250$  GeV, Compton scattered electrons from  $E = 44$  GeV down to the Compton edge at  $E = 25$  GeV can be detected in this setup. The accessible spectrum is spread over a distance of approximately 13 cm. Due to the expected background, detection methods insensitive to photons and with an intrinsic energy threshold for charged particles are considered advantageous.

## 2.3 Detectors for the ILC Compton Polarimeters

A natural choice for fast counting detectors are Cherenkov detectors read-out by a photomultiplier. For relativistic electrons, this detection mechanism is intrinsically linear, since the amount of emitted Cherenkov light is proportional to the number of electrons passing through that channel. Depending on the choice of Cherenkov medium, the threshold for Cherenkov radiation can be in the MeV regime, which suppresses backgrounds from low energetic electron-positron pairs from beamstrahlung. This is in particular true for gases with refractive indices only slightly above unity. E.g. for  $C_4F_{10}$  with  $n = 1.0014$ , the Cherenkov threshold is at 10 MeV. Due to their reliability, robustness and proven performance in the so far most precise Compton polarimeter which measured the polarisation of the electron beam at SLC [11], gas Cherenkov detectors are considered the default solution for the ILC polarimeters. As will be discussed below, the detector linearity is one of the most important systematic uncertainties of this type of detector. Therefore, we present in this paper a calibration system which is suitable to detect and correct for nonlinearities at the sub-percent level in-situ.

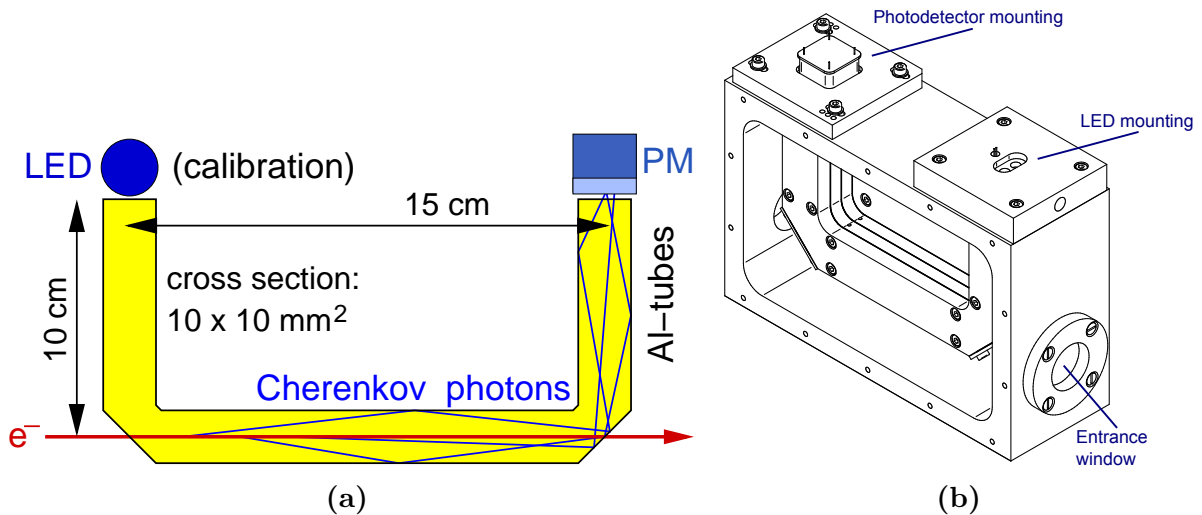
Recently, a Cherenkov detector for polarimetry based on quartz has been proposed [20]. With a much higher light yield (due to the higher refractive index) in combination with a higher granularity, such a system would be robust against nonlinearities up to the percent-level. However, this concept still awaits a full demonstration in testbeam and a full evaluation of the robustness against backgrounds, since the Cherenkov threshold is much lower.

Ultimate granularity would be achieved with a silicon pixel detector, eliminating the question of linearity completely and increasing significantly the possibilities to control the alignment. However, in this case R&D is still required to reach a proof-of-concept level, where the main concern is the high local data rate in the most intense region of the Compton spectrum, followed by radiation issues.

### 2.3.1 A Gas Cherenkov Detector for Compton Polarimetry

A prototype of a gas Cherenkov detector for ILC polarimetry has been designed, built and operated successfully in testbeam [9]. Based on the experience gained at SLC, the design of the channels has been improved to U-shaped aluminium tubes with a square cross section of  $1 \times 1$  cm. A schematic side view of one channel is depicted in Figure 3a.

When the electrons traverse the horizontal tube of the Cherenkov counter, they induce Cherenkov light. Mirrors at the end of the tube reflect the Cherenkov light upwards such that the actual photo detector can be placed outside the Compton scattering plane. The other upward pointing “leg” of the U-shaped channels is foreseen to host an LED-based calibration system. For the upstream polarimeter, 20 such channels would be staggered along the shallow angle exit window.



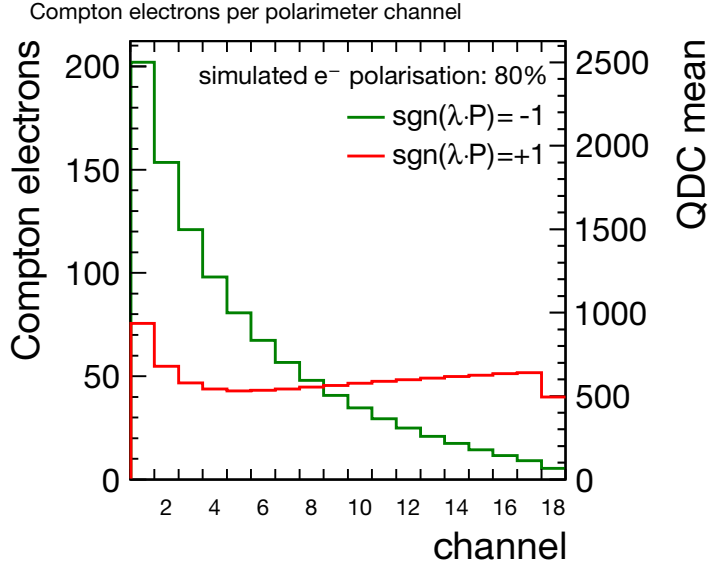
**Figure 3:** (a) Schematic drawing of one gas Cherenkov detector channel. (b) Picture of the two-channel Gas Cherenkov detector prototype. Both from [9].

Figure 3b shows a drawing of the prototype which consists out of two non-staggered channels. In testbeam, it was demonstrated that the aimed detector alignment goals can be achieved, in particular when multi-anode photomultipliers (MAPMs) are used which allow to measure asymmetries in light distribution in each channel. Since the light pattern on the detector plane is related to the detector–beam alignment, the alignment can also be measured and monitored during a physics run without spending dedicated beam time on alignment runs [9].

Figure 4 shows the number of expected Compton scattered electrons per polarimeter channel for a simulated polarisation of  $\mathcal{P} = 80\%$ , as obtained from the fast Linear Collider Polarimeter Simulation LCPo1MC [4, 21]. The axis on the right-hand side illustrates the expected QDC signal assuming the parameters of the prototype detector [9], thus a light yield of  $\eta = 6.5$  photoelectrons/ Compton electron, a photomultiplier gain of  $g = 3.0 \times 10^5$  and a QDC resolution of 25 fC/QDC count.

### 2.3.2 Sources of Systematic Uncertainties

In the multi-event mode, the statistical uncertainty of the polarisation measurement drops rapidly such that already after a few seconds of data taking, the polarisation measurement uncertainty is dominated by systematic uncertainties. Table 1 summarises the envisaged error budget at the ILC in comparison to the obtained systematic uncertainties at the SLC polarimeter [11].



**Figure 4:** Simulated number of Compton scattered electrons per polarimeter channel for the different laser helicities. The right axis shows the expected QDC signal assuming the parameters of the prototype detector, see text.

source of uncertainty	$\delta\mathcal{P}/\mathcal{P}$	
	SLC	ILC goals
laser polarisation	0.1%	0.1%
detector alignment	0.4%	0.15 – 0.2%
detector linearity	0.2%	0.1%
electronic noise and beam jitter	0.2%	0.05%
Total	0.5%	0.25%

**Table 1:** Error budget of the polarisation measurement at the ILC [4] in comparison to the determined systematic uncertainties at the SLC polarimeter [11].

**Laser polarisation.** The laser polarisation and its flip accuracy have been controlled to the level of 0.1% already at the SLC polarimeter. Currently, no improvement is envisaged for the ILC case.

**Noise & jitter.** Contributions originating from electronic noise, which were sizeable at the time of the SLC polarimeter, are expected to be negligible for modern DAQ hardware as applied in the ILC polarimeters, which is confirmed by the testbeam experience with the prototype [9]. Also the beam jitter is expected to be significantly reduced in the ILC case, since the luminosity goals require to limit the jitter to at most 10% of the beam sizes [2].

**Analysing power.** At cross-section level, the analysing power can be calculated with high precision from the Compton cross section known currently to the order  $\alpha^3$  [10]. Therefore, the knowledge of the analysing power is dominated by the alignment of the detector with respect to the Compton spectrum, which includes lateral shifts of the Compton IP as well as the finite knowledge of the magnetic fields of the

chicane. Both effects are included when the alignment is derived from measuring the unpolarised Compton spectrum, e.g. from the sum of data taken with the two laser helicities. The foreseen error budget translates into a vertical alignment precision of at least  $100\ \mu\text{m}$  and a precision of the tilt angle of the detector of  $1\ \text{mrad}$  with respect to the design beam orbit [20]. A granularity of about  $1\ \text{cm}$  provides sufficient detail to achieve this level of control by monitoring the shape of Compton spectrum [9]. It has been shown that the requirements for shifts as well as tilts of the detector could be met with the prototype, in particular when assisted by information of the intra-channel light pattern read-out by multi-anode PMTs [9].

**Detector nonlinearities.** Apart from the alignment, the detector nonlinearities are the other source of uncertainty which needs to be improved significantly in order to meet the precision goal for the ILC. From equation (7), it becomes clear that a polarimeter detector does not need to be calibrated on an absolute scale, since any constant calibration factor cancels. However, the linearity of the detector response is essential for per mille-level polarimetry.

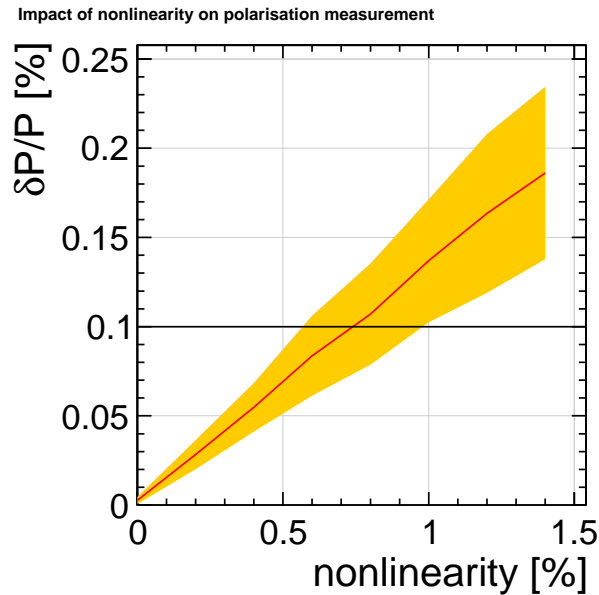


**Figure 5:** Systematic uncertainty on polarisation measurement due to different detector nonlinearities. The error band shows the RMS interval obtained from 200 randomly chosen detector response functions. The exact definition of nonlinearity employed here is described in section 3.1.

In order to investigate the maximal tolerable detector nonlinearity which still keeps the nonlinearity contribution to the overall systematic uncertainty below  $0.1\%$ , the impact of different nonlinear detector response (or transfer) functions on the measurable polarisation has been studied in Monte Carlo simulations. For each value of the relative nonlinearity, 200 third order polynomials with random parameters have been generated and applied as transfer functions in the simulated polarisation measurement. The results are depicted in Figure 5. The red line indicates the absolute value of the mean deviation between the reconstructed and true polarisation,

while the yellow band shows the RMS of those samples. It becomes obvious that the detector nonlinearity must be controlled at the level of 0.5% in order to keep the resulting contribution to  $\delta\mathcal{P}/\mathcal{P}$  below 0.1%. A method to achieve this is discussed in the next chapter.

### 3 A Calibration System for the ILC Polarimeters

In order to control the detector nonlinearity on a level of below 0.5%, novel calibration techniques are needed. In this section, we present a calibration system, which is capable to meet these requirements.

#### 3.1 Definitions of Nonlinearity

Basically, there are two ways of describing the nonlinearity of a detector, which are illustrated in Figure 6: The integrated nonlinearity (INL) specifies the absolute deviation of the detector response  $T(x)$  from a linear response  $L(x)$ , where  $x$  is an applied signal (c.f. Figure 6a). Thereby, the linear response is defined by the response to a signal  $x_{\text{ref}}$  which marks the end of the range to be calibrated.

Another way of describing a nonlinearity is the differential nonlinearity (DNL). Here, the deviation between the slope of the detector transfer function and the linear response is used (c.f. Figure 6b). Although the DNL does not preserve any information about the absolute scale of the detector response, all the information regarding the linearity of the response is still present. Thus, also a DNL measurement can be used to linearise the detector response.

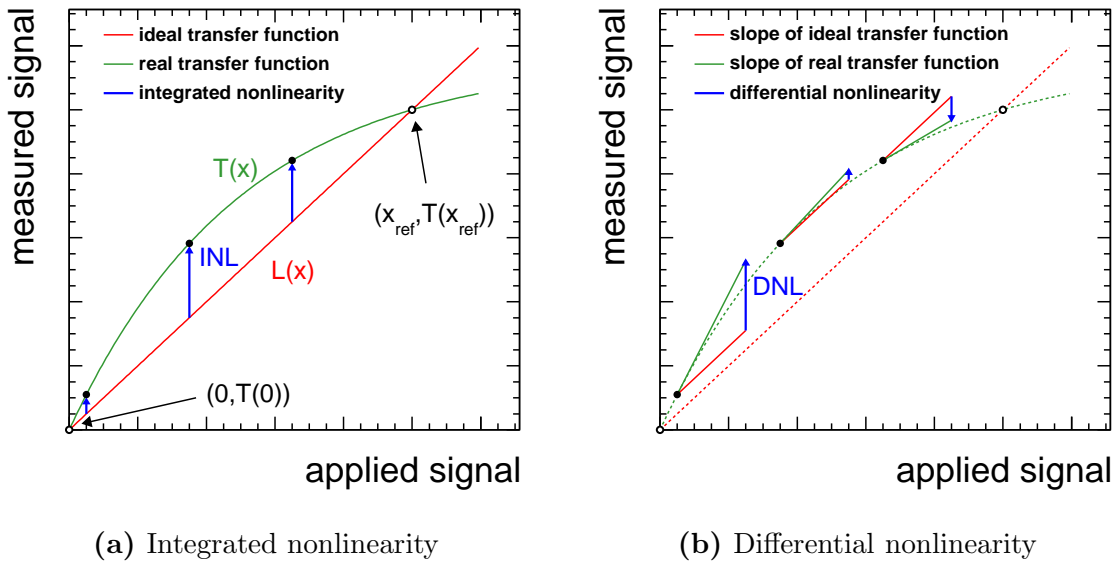


Figure 6: Different ways of specifying the nonlinearity of a detector response.

## 3.2 Permille-Level Linearisation

Measuring the nonlinearity of a light detector to permille-level is very challenging as this usually requires an intensity calibrated light source of the same precision. Different calibration methods based on LED light pulses were studied in Reference [22]. In the following, we will focus on a double pulse method, which pursues a differential calibration approach: One light pulse (base pulse  $x$ ) is tunable in its light intensity over the expected dynamic range of the detector. A second light pulse (differential pulse  $\Delta x$ ) features a constant intensity, which is small compared to the dynamic range. Measuring the detector response to  $x$  and  $x + \Delta x$ , allows to estimate the DNL. This approach is advantageous as it does not require a calibrated light source at all as it will be demonstrated in the next section. Details on this method are also discussed in Reference [23].

### 3.2.1 Mathematical Foundations and Linearisation Method

In the following, we outline the mathematical foundations and the procedure of permille-level linearisation using the double pulse method.

The most general transfer function of a detector can be parametrised as

$$T(x) = A + (B + nl(x))x. \quad (9)$$

Herein,  $A$  denotes an offset (e.g. due to dark current), which can be easily measured and subtracted. Thus, we set  $A = 0$  for simplicity.  $nl(x)$  is an arbitrary function which describes the nonlinear part of the detector response. In order to linearise the detector response, the correction function

$$\text{Corr}(x) = \frac{B}{B + nl(x)} \quad (10)$$

needs to be determined.

The derivative of  $T(x)$  is proportional to the difference between the values of the detector response for a dedicated light signal  $x$  and the signal which is increased by a constant and small additional quantity of light from the differential light pulse  $\Delta x$ :

$$D(x) := \frac{d}{dx} T(x) \approx \frac{\Delta T(x)}{\Delta x} \propto \Delta T(x) = T(x + \Delta x) - T(x) \quad (11)$$

If  $nl(x)$  is small, which is intrinsically the case for photomultipliers, it holds

$$D(x) \propto D(T(x)) \propto \Delta T(T(x)). \quad (12)$$

Thus, measuring  $\Delta T$  in dependence of  $T(x)$  contains (up to a proportionality factor) approximately the same information as the direct derivative of the transfer function in dependence of the absolute amount of injected light  $x$ . Thus, we achieve an approximate determination of the derivative of the transfer function which does not rely on the

knowledge of the injected quantity of light  $x$ , but only on the corresponding detector responses.

The measurement of the data pairs  $(T(x), \Delta T(T(x)))$  can now be used to build the correction function  $\text{Corr}(x)$ . For this purpose, the data points are fitted with a higher order polynomial in order to obtain a continuous function which can then be processed further.

Combining Equations (9) and (11) gives

$$\Delta T(x) \approx \Delta x \cdot \frac{d}{dx} T(x) = \Delta x \cdot (B + nl(x) + nl'(x)x). \quad (13)$$

Thus, the average of  $\Delta T$  over the whole dynamic range can be identified as

$$\langle \Delta T(x) \rangle = \Delta x \cdot (B + \langle nl(x) + nl'(x)x \rangle) = \Delta x \cdot B. \quad (14)$$

Note that the average over the  $nl(x)$ -dependent terms in Equation (14) vanishes, as by definition  $nl(x_{\text{ref}}) = 0$ :

$$\frac{1}{x_{\text{ref}}} \int_0^{x_{\text{ref}}} (nl(x) + nl'(x)x) dx = \frac{1}{x_{\text{ref}}} [nl(x)x]_0^{x_{\text{ref}}} = 0. \quad (15)$$

In a next step, Equation (13) is corrected for the constant part

$$\Delta T(x) - \Delta x \cdot B \equiv \Delta \hat{T}(x) = \Delta x(nl(x) + nl'(x)x) \quad (16)$$

and  $\Delta \hat{T}(x)$  is integrated in order to obtain an expression for  $nl(x)$ :

$$\frac{1}{x} \int_0^x \Delta \hat{T}(x') dx' = \Delta x \cdot nl(x) \quad (17)$$

Finally, Equation (14) and (17) can be combined in order to construct the correction function of Equation (10). The remaining proportionality factor  $\Delta x$  in (14) and (17) cancels. It should be stressed once more that  $\text{Corr}(x) \approx \text{Corr}(T(x))$  can be determined without knowing the absolute input light signal. The only requirement is that the additional quantity of light  $\Delta x$  is constant and small compared to the quantity of light  $x$  which scans the dynamic range.

### 3.2.2 Monte-Carlo Study

In order to test the presented linearisation method, a Monte-Carlo simulation has been developed, which takes into account the simulation of the light emission, attenuation, detection, and digitisation. The simulation parameters have been taken from datasheets of the foreseen DAQ equipment or, in case of the light source parameters, have been adjusted in agreement with measured distributions. With this simulation, the performance and limitations of the described linearisation method can systematically be studied and parameters for a measurement setup can be optimised.

As the desired linearisation is in the sub-percent range, a sufficiently large number of data points ( $T(x), \Delta T(T(x))$ ) with a sufficiently large statistic needs to be acquired. From the simulation we find that the number of scan steps within the dynamic range plays a small role as long as it exceeds four scan steps. This can be understood since nonlinear contributions of higher orders in the transfer function play a decreasing role and, thus, more data points do not strongly constrain the polynomial fit anymore. However, in order to ensure a good modelling of the nonlinearity by the fit it is advantageous to adjust the number of scan steps according to the time budget of a nonlinearity measurement. A much stronger influence on the performance of the linearisation method has the number of measurements taken at one scan step since this affects the statistical uncertainty of the individual data points. It has been found that in order to allow for a sub-percent linearisation at least  $3 \times 10^6$  measurements per scan step are desirable.

One key requirement is the stability of the differential light pulse. Figure 7 shows the impact of a drift of the intensity of the differential pulse by 0.2% and 2.0% within the scan range on the resulting nonlinearity before and after the linearisation. This figure illustrates that for small drifts the detector response can still be well linearised. However, once the drift gets too large the linearisation method does not work satisfactory anymore. In order to estimate the maximal tolerable drift of the differential pulse, this parameter

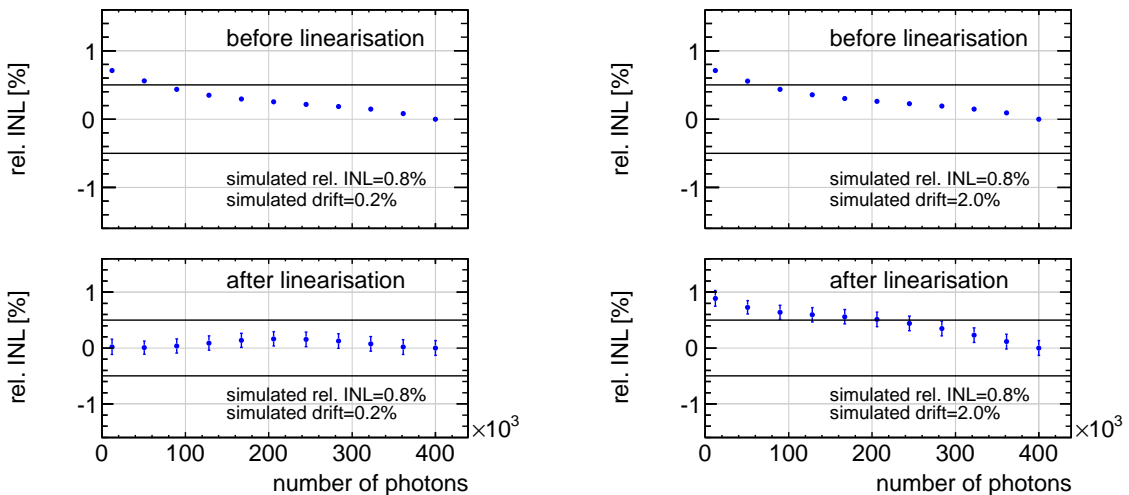


**Figure 7:** Simulation of the effect of 0.2% and 2.0% drift in the light intensity of the differential pulse during the scan of the dynamic range. The horizontal line indicates the design goal of a nonlinearity smaller than 0.5%. For a too large drift, the method does not sufficiently linearise the detector response anymore.

has been scanned in the simulation. Thereby, for each scan step, 200 randomly generated nonlinear transfer functions featuring the same total integrated nonlinearity of 0.8% but different shapes have been simulated. Figure 8 shows the average effective nonlinearity, defined as  $INL_{\max} - INL_{\min}$  in the studied range, after the linearisation. The uncertainty band indicates the RMS of the resulting distribution around the central value. From the figure it gets clear that the differential pulse must not drift by more than 0.5% during the scan of the dynamic range in order to still fulfil the goal of a linearisation better than 0.5%.

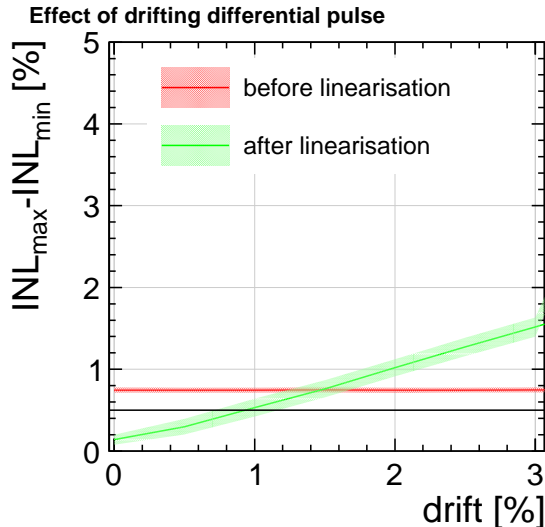


**Figure 8:** Effective nonlinearity in dependence of different simulated drifts of the differential pulse. The drawn error band shows the RMS around the mean value from all 200 simulated shapes of nonlinearities. In order to keep the resulting nonlinearity below 0.5%, the differential pulse must not drift by more than 0.5%.

The presented linearisation method is based on the assumption of only small detector nonlinearities (cf. Equation (12)). Therefore, also the limitations of the method with respect to the underlying nonlinearity needs to be studied. Figure 9 shows the effective nonlinearity before and after linearisation for different simulated nonlinearities. One can see that nonlinearities of up to 3.5% can still be corrected successfully with the proposed approach such that the effective nonlinearity stays below 0.5%. This range is sufficient for photomultipliers, which are intrinsically very linear devices.

### 3.3 Requirements for the calibration system

The differential calibration approach has the advantage that the requirements for the calibration light source is reduced. However, it still needs to fulfil a few specifications:

**General design.** The calibration system must consist of two independent light sources, which can be independently adjusted in their light intensity.

**Stability of differential pulse.** The light pulse of the differential pulse defines the measure of the derivative and, therefore, it must be very stable. In the previous section it has been shown that a relative drift of the differential pulse of 0.5% is tolerable in order to still meet the calibration requirements.

**Dynamic range of base signal.** The light source providing the base pulses has to be adjustable in its light intensity over the whole dynamic range of the planned Compton polarimeters in order to be able to probe the differential nonlinearity within this range. As can be seen from figure 4, up to 200 Compton electrons per bunch crossing

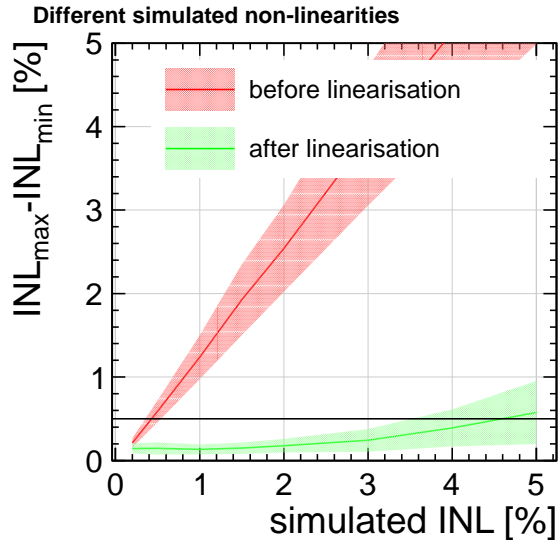


**Figure 9:** Effective nonlinearity in dependence of the simulated relative INL. The drawn error band shows the RMS around the mean value from all 200 simulated shapes of nonlinearities. The proposed linearisation method still works for a relative INL of up to 3.5%.

can be expected in a single detector channel, assuming the nominal instantaneous Compton luminosity.

Additionally, there are some more requirements, which are important in order to meet the conditions of the actual polarisation measurement at the ILC.

**Wavelength.** The light sensors at the Compton polarimeters are supposed to detect Cherenkov light, whose wavelength intensity distribution peaks in the UV range. Therefore, the calibration light source should emit light in this wavelength range as well.

**Short pulses.** An ILC bunch with a longitudinal bunch length of  $300 \mu\text{m}$  [2] traversing the Compton polarimeters creates a Cherenkov light pulse of only  $t = 1 \text{ fs}$ . This is much shorter than the usual transit time of the electron avalanche in a photomultiplier. Therefore, the light pulse of the calibration source should be as short as possible, but at least as short as the photomultiplier transit time, which is of the order of  $10 \text{ ns}$  for photomultipliers we consider in our setups.

**Applicable in detector design.** The light source should ideally be very small such that it can be integrated in the existing polarimeter design.

### 3.4 LED driver

According to these specifications an LED driver has been developed based on the calibration light source of the CALICE tile hadron calorimeter [24]. Figure 10a shows a picture of the LED driver. It is equipped with two UV-LEDs which feature a peak intensity at

$\lambda = 395 \text{ nm}$  and a rather large spectral width of a few 10 nm. The LED light intensity is defined by two external reference voltages  $U_{\text{LED}1,2}$ . Both LEDs receive the same trigger signal.

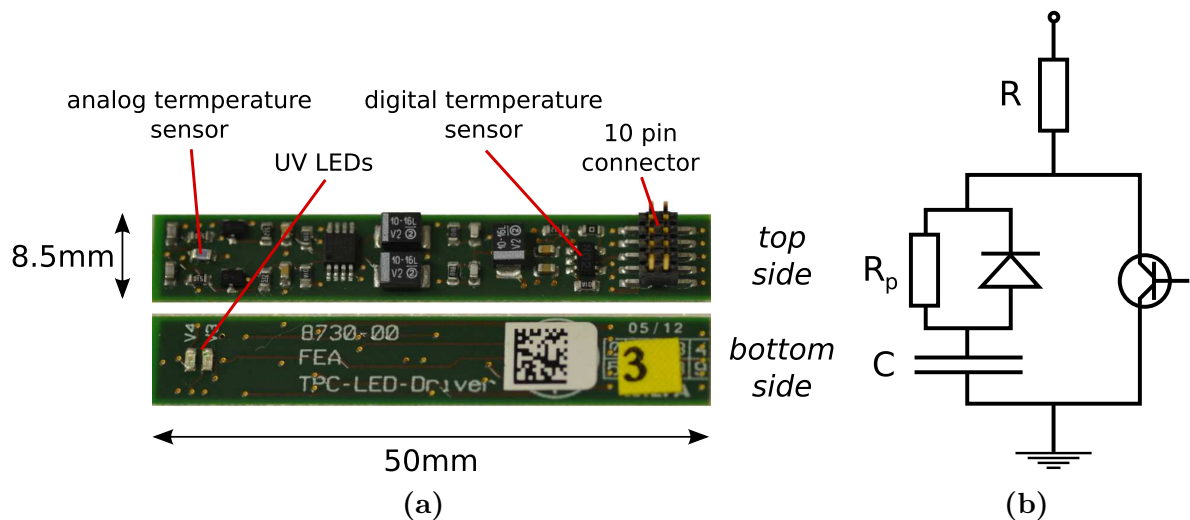


**Figure 10:** (a) Picture of the LED driver. The design is chosen such that it is applicable in the gas Cherenkov detector design. (b) LED driver circuit.

It is eye-catching that the dimensions of the board are rather small ( $50 \times 8.5 \text{ mm}^2$ ) such that the driver can easily be integrated in the existing Cherenkov detector design (see section 2.3.1). Both UV-LEDs are located on the bottom side of the board, whereas the remaining electronic components are placed on top. As LEDs are rather temperature dependent devices, two temperature sensors are located on the board. An analogue temperature sensitive resistor (Pt1000) is placed directly opposite the LEDs on the top side. A second, digital temperature sensor (DS18B20U) is present at the other end of the board, which provides a 12-bit digitised temperature, read out via a 1-wire bus. The board is connected via a 10-pin connector.

A simplified schematic of the LED driver circuit is shown in Figure 10b. This design [24] allows for very short light pulses. There are three phases in the generation of a light pulse: Firstly, the capacitor  $C$  gets charged via the resistors  $R$  and  $R_p$  ( $R \gg R_p$ ) driven by the external voltage  $U_{\text{LED}}$ . Secondly, when the trigger arrives, the transistor is closed and the capacitor discharges via  $R_p$  and  $R_{\text{LED}}$ . The LED is emitting light. Thirdly, the resistance of the LED rises as the voltage at the capacitor drops due to the nonlinear  $I - V$  behaviour of the LED. The discharging continues mainly via the parallel resistor  $R_p$  and, thus, the LED light pulse is quenched.

The LED board has been carefully characterised in a dedicated test setup. Figure 11 shows a schematic overview of the setup. It consists of a light tight box with an optical bench inside, on which the LED driver as well as a photomultiplier is mounted. As photodetector a segmented photomultiplier by Hamamatsu (R5900-03-M4) has been selected. This type has also been operated in the gas Cherenkov detector prototype described in section 2.3.1. For a coarse adjustment of the light intensity, different neutral density filters can be inserted into the optical path. In the standard setup, the photomultiplier is read out by a 12-bit QDC.

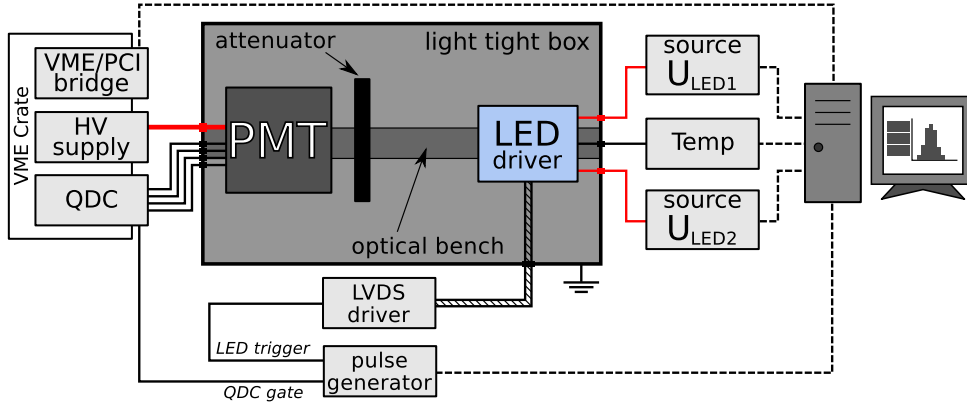


**Figure 11:** Schematic picture of test setup for characterising the LED driver board and for measuring the differential nonlinearity of a photomultiplier.

In order to resolve the pulse length of light pulses emitted by the LED driver, the photomultiplier has been connected to an oscilloscope at first. Figure 12a shows the recorded wave forms for different reference voltages  $U_{\text{LED}}$  averaged over 5120 individual light flashes. It is visible that the measurable pulse length is below 10 ns and, thus, the driver fulfils the described pulse length requirement. The observable wiggles at  $t > 40$  ns can be attributed to photomultiplier after pulses and signal reflections because of imperfect signal termination at the oscilloscope. In order to exclude those nonlinear effects from the QDC measurements it is important to choose the gate carefully.

In Figure 12b, a QDC measurement of the dynamic range of the LED driver is depicted. From Monte-Carlo simulations it is known that at the ILC polarimeters signals of up to 3000 QDC counts are expected in the most extreme detector channels (c.f. Figure 4). Thus, Figure 12b proves that the expected dynamic range can completely be covered by the LED driver. Furthermore, the dynamic range of the LED driver can be adjusted easily with different filter configurations if needed.

In order to test the stability of the base pulse, the PMT response to light pulses at different fixed LED reference voltages has been measured for about one hour each. Figure 13 displays two of these measurements at different voltage levels. The data points represent the pedestal corrected mean positions of a QDC spectra corresponding to  $N = 10^5$  light flashes, thus  $T(x)$  in the terminology introduced in section 3.2. In Figure 13a, the reference voltage has been set from a higher level to  $U_{\text{LED}} = 6.0$  V. In contrary, in Figure 13b the voltage level has been raised from a lower level to  $U_{\text{LED}} = 6.5$  V. A dragging behaviour in opposite directions can be observed in the figures although the reference voltage was constant. After about 40 minutes the light intensity stabilises. This is important to note, since for the proposed nonlinearity measurement the base pulse is altered every few minutes. In order to achieve reliable results for the nonlinearity measurement, the base pulse should always be scanned in both directions such that the dragging effect can be cancelled by averaging.

The differential pulse stability has been checked on the absolute scale for 12 hours, which corresponds roughly to the time of a full nonlinearity measurement run in the shown setup. A drift of at maximum 0.41% has been observed, which is within the tolerable range according to Monte-Carlo simulations (see Section 3.2.2).

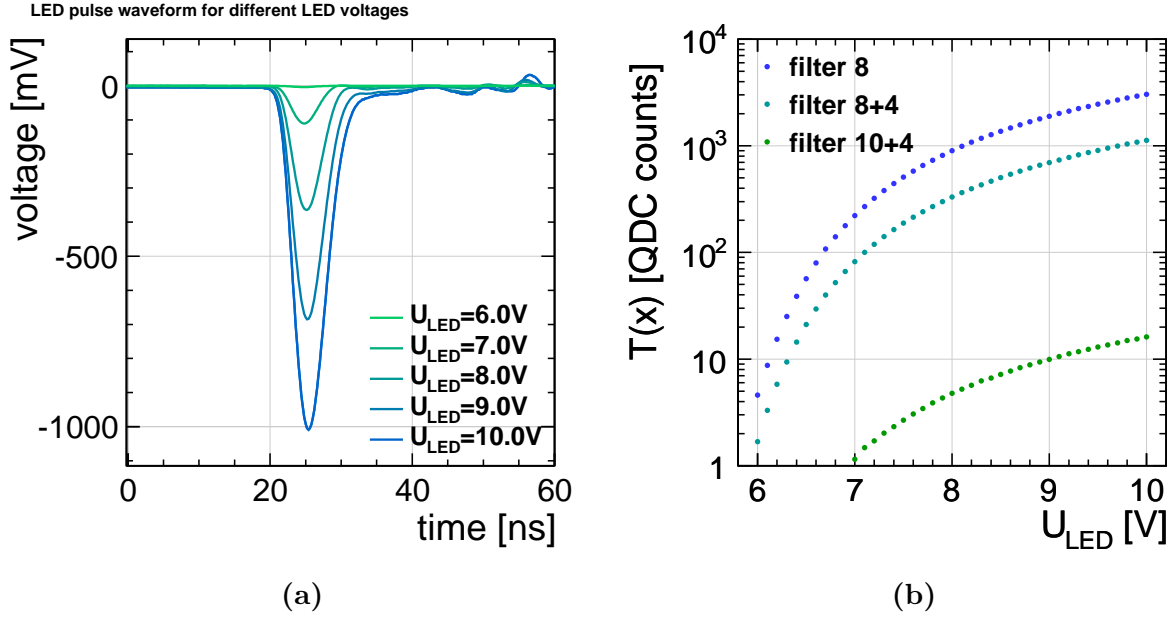


**Figure 12:** (a) Recorded waveforms of the photomultiplier response for different reference voltages. The pulses are shorter than 10 ns. (b) Dynamic range of the LED driver for different filter configurations. The expected dynamic range of the ILC polarimeter can be covered.

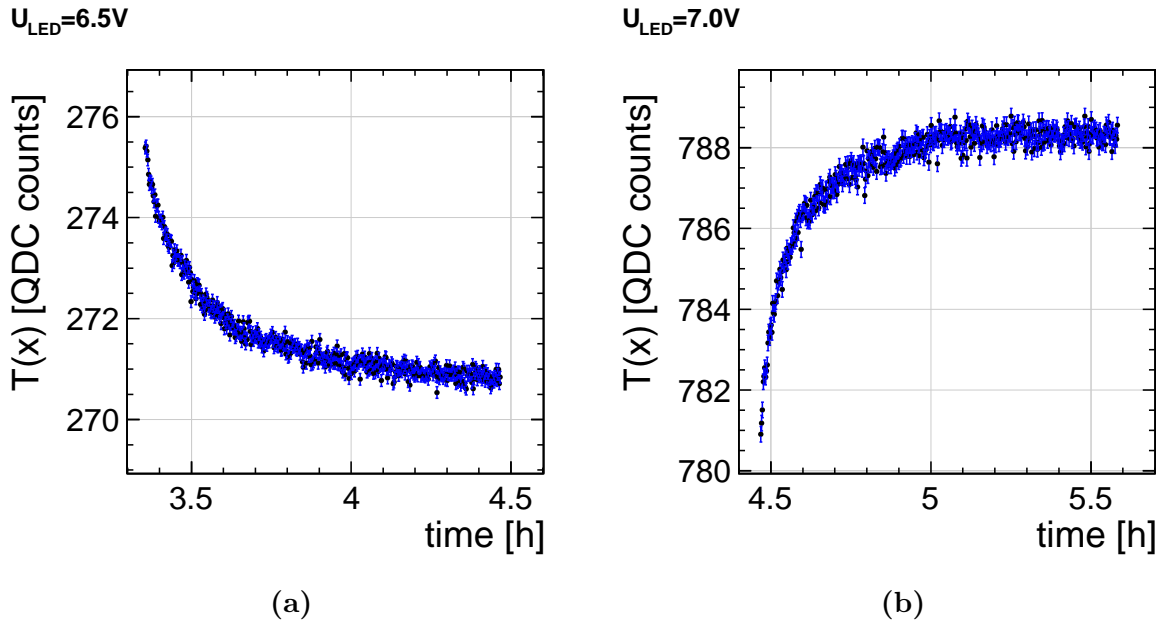


**Figure 13:** Pedestal corrected mean position of the QDC spectra for changing LED voltages  $U_{LED} = 6.5 V$  and  $U_{LED} = 7.0 V$ . About 40 minutes after a voltage change a stable mean position is reached.

During the tests it has been observed that the differential pulse intensity depends on the base pulse voltage level. In order to avoid this cross talk for the following nonlinearity measurements, two independent LED driver boards have been used. In this modified

setup, only one LED per LED driver board has been used. The other LED on the boards has been set to  $U_{\text{LED}} = 0 \text{ V}$ .

Except from the cross-talk problem, the LED driver has proven to fulfil the requirements for the usage in the proposed differential nonlinearity measurement. In a future design, the two LEDs on one board will be operated in independent circuits.

## 4 Measurement Results and Application to the ILC

In this section, we present a measurement of the nonlinearity for one of the PMTs used in the prototype detector, and we discuss the implications for ILC polarimetry.

### 4.1 Nonlinearity measurements

With the setup described in section 3.4 we determined the nonlinearity of one of the candidate PMTs to be employed in the Cherenkov detectors of the ILC polarimeters. Figure 14a shows the result of a differential nonlinearity measurement of the photomultiplier R5900-03-M4 operated at 700 V. For each voltage setting of the base LED, responses  $T(x)$  to the base pulse alone and  $T(x + \Delta x)$  to base and differential pulse together are determined from  $10^5$  samples each.

As already discussed, a slightly different  $\Delta T(x) = T(x) - T(x + \Delta x)$  is obtained depending on the scan direction of the base pulse. The black data points show the average of both scan directions, which is used to determine the relative nonlinearity in Figure 14b. Since the nonlinearity is defined with respect to the detector response at the end of the dynamic range, the nonlinearity vanishes at this point by construction. It can be observed qualitatively that the detector response starts to show a saturating behaviour, which is expected for photomultipliers at high light intensities. The measurement has been repeated with different filter configurations and exchanged hardware and all measured nonlinearities are in agreement with the presented one [23].

The measured nonlinearity can now be used for deriving a correction function. In order to demonstrate the correction power of this method, an independently measured data set has been linearised using the correction function. Thereby, all base+differential and base pulse measurements have been individually corrected and from this corrected data  $\Delta T(x)$  has been calculated again. Figure 15a shows  $\Delta T(x)$  with respect to the base pulse mean position before and after the application of the linearisation algorithm. It is clearly visible that after the linearisation the data points for  $\Delta T(x)$  are much more consistent with a constant than before. Figure 15b visualises the originally measured nonlinearity as well as the residual nonlinearity after correction, which is more than a factor 5 smaller than before the correction.

This demonstrates that the LED driver, the nonlinearity measurement and the linearisation method are suitable to measure and correct PMT responses at the sub-percent level.

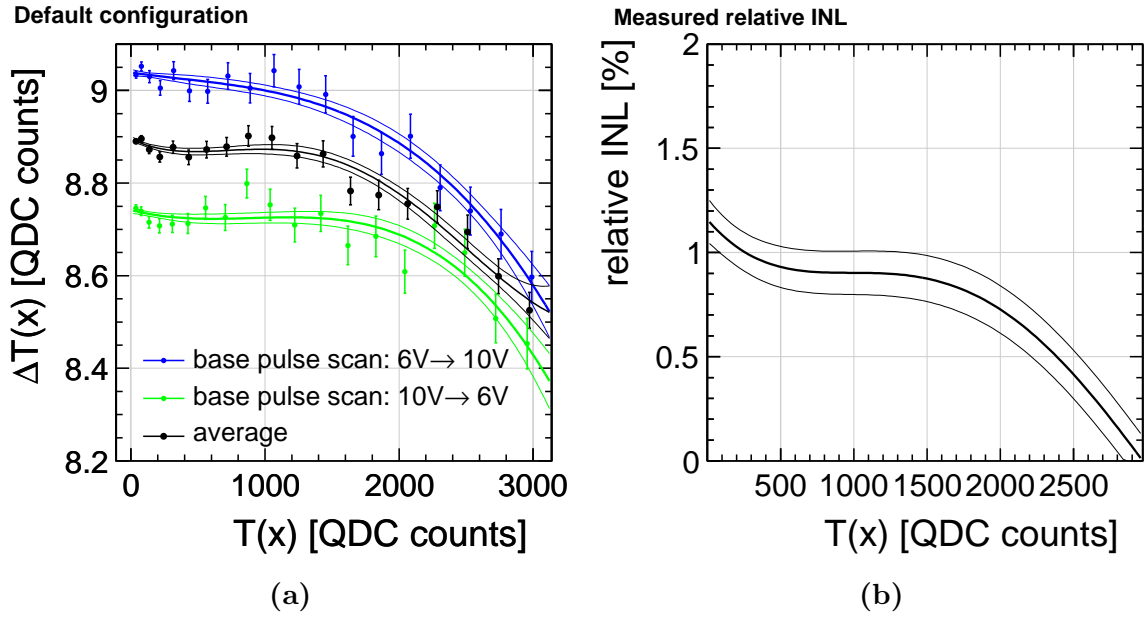


**Figure 14:** (a) Measured  $\Delta T(x)$  in the default configuration for different scan directions of the base pulse. (b) Determined relative INL. The absolute scale is not accessible with the presented method.

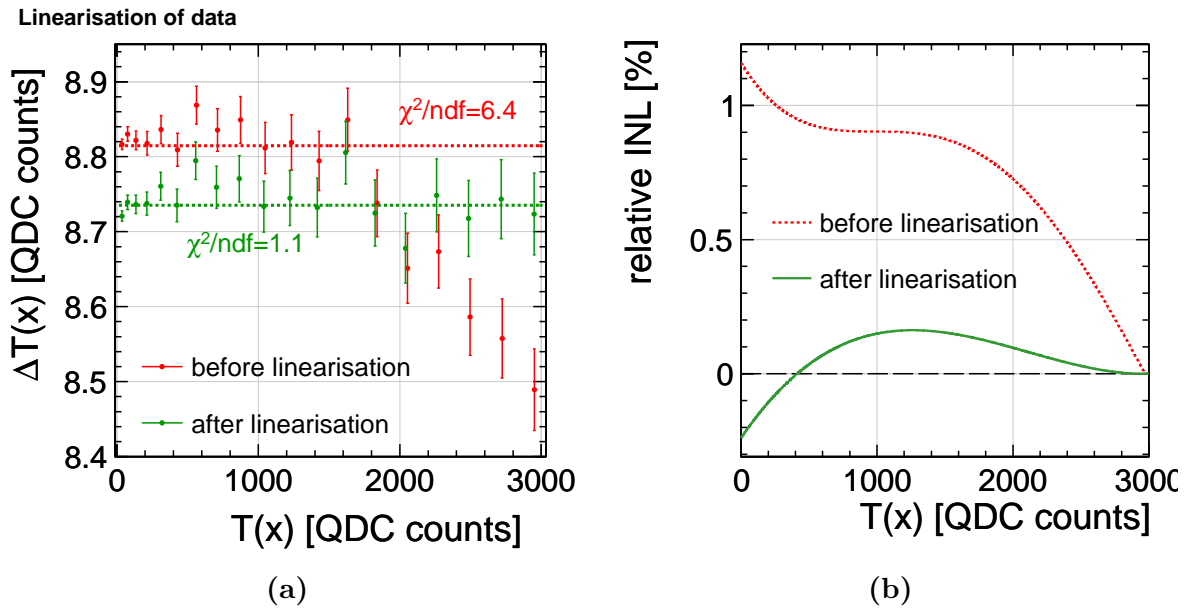


**Figure 15:** (a) Independent data set before (red) and after (green) linearisation. (b) Visualisation of the measured nonlinearity from Figure 14b and the residual nonlinearity after the linearisation. Linearity has been improved by about a factor of 5.

## 4.2 Application to Polarimetry

As a final step, we consider the application to the ILC situation. For this purpose, the measured nonlinearity from figure 14b has been applied within the fast Linear Collider Polarimeter Simulation LCPolMC [4, 21]. Figure 16 shows the polarisation calculated in each detector channel according to equation 7, based on three different estimators for the number of Compton electrons  $N$ : The true number of Compton electrons (blue,  $P_{\text{C.e.}}$ ), the mean values of the QDC spectra simulated with the measured nonlinearity from figure 14b (red,  $P_{\text{meas}}$ ) and with the residual nonlinearity after correction as shown in figure 15b (green,  $P_{\text{corr}}$ ). In addition, the combined polarisation measurement obtained from the weighted mean of the per-channel polarisations according to equation 8 is given in figure 16.

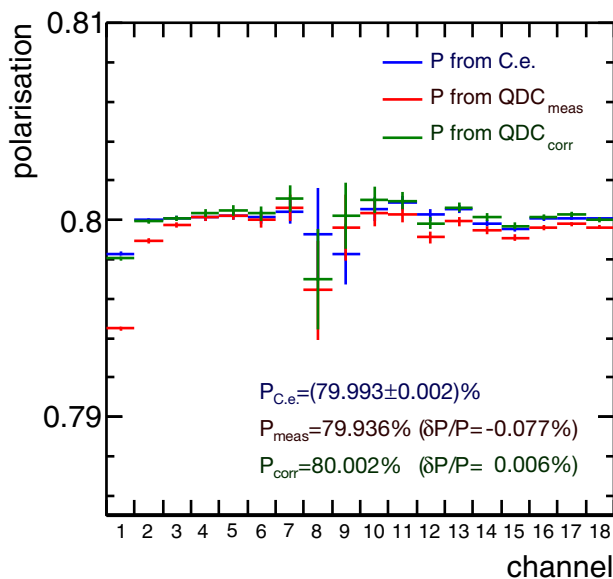


**Figure 16:** Simulation of a polarisation measurement with the ILC upstream polarimeter based on the true number of Compton electrons per channel (blue,  $P_{\text{C.e.}}$ ), the mean values of the QDC spectra simulated with nonlinearity (red,  $P_{\text{meas}}$ ) and after applying the correction (green,  $P_{\text{corr}}$ ).

In this particular case, the measured nonlinearity causes a deviation of only  $|\delta\mathcal{P}/\mathcal{P}| = 0.08\%$ , which would still be within the envisaged uncertainty budget. Comparison with figure 5 shows, however, that the nonlinearity measured for this specific PMT has a rather benign shape, since for an INL of 1% a mean deviation of  $|\delta\mathcal{P}/\mathcal{P}| = 0.14\%$  is expected, with an RMS of  $\pm 0.4\%$ .

Considering the channel-dependency, the measured polarisation values are most obviously distorted in the channels with large absolute differences between the count rates for parallel and opposite laser and beam helicities, i.e. at small channel numbers. While at a first glance it could be argued that channels which measure a polarisation different from the average could simply be excluded, a closer look reveals that this is not sufficient: For all channels with a significant statistical weight, and especially those above the zero crossing of the asymmetry (channel numbers larger than 10), the uncorrected polarisation (red)

is consistently smaller than the value expected from the number of Compton electrons (blue). Furthermore, the dependence of the measured polarisation on the channel number is not a unique indicator for the presence or absence of nonlinearities, but can also be influenced by misalignments or tilts between detector and beamline [20]. Thus, the differential nonlinearity measurement is essential for a precise monitoring of the detector nonlinearity and its separation from other effects.

After applying the determined correction to the QDC mean values, the obtained channel-wise polarisation values  $P_{\text{corr}}$  (green) reproduce the reference values from the “true” numbers of Compton electrons nearly perfectly. This lays the foundation to disentangle effects due to nonlinearities from others caused e.g. by the above-mentioned misalignments and tilts in a real polarimeter system. The relative deviation of the average polarisation from the Compton electron-based value becomes 0.006 %, thus more than a factor ten smaller than before, and a factor 16 smaller the effect foreseen in the uncertainty budget in table 1. This shows that the linearisation based on our test setup would be fully sufficient for the ILC polarimeters, and even has the potential to reduce the impact of nonlinearities to a negligible level.

Beyond a careful initial characterisation of the photomultipliers in the lab before the actual installation in the ILC polarimeters, an in-situ monitoring of the detector calibration is clearly required to maintain the achieved precision over many years of ILC operation. A possible measurement scheme at the ILC during a run is depicted in Figure 17. It makes use of the pulsed beam structure at the ILC in which each bunch train is separated in time by 199 ms. The polarimeters are idle in this time such that this period can be utilised for calibration measurements. Operating the LEDs at different frequencies  $f_{\text{LED1}} = 2f_{\text{LED2}} = 30$  kHz would allow for measuring  $N = 2388$  data points ( $T(x); \Delta T(x)$ ) assuming that 80% of the time between two trains can effectively be used. In order to reach the demanded precision,  $N = 3 \times 10^6$  data points per base pulse voltage have to be acquired (c.f. Section 3.2.2), which is possible within less than 5 minutes. Thus, the whole dynamic range could be scanned back and forth in 10 steps within less than 1.5 hours in parallel to a normal ILC physics run.

In order to make this operation mode possible, small modifications of the LED driver board are necessary: Obviously, it must be synchronised with the ILC clock. Furthermore, both LEDs need to be able to be triggered independently, which can be easily realised in the current design. This decoupling of the trigger circuit could also solve the observed cross talk between the two LEDs.

## 5 Conclusions

In this paper, we presented a calibration system for the Compton polarimeters at the ILC. The baseline technology to measure the Compton scattered electrons is a gas Cherenkov detector, read-out by single- or multi-anode PMTs. One of the key performance parameters is the linearity of such a detector. In order to keep the corresponding contribution to the systematic uncertainty of the polarisation measurement below 0.1 %, the nonlinearities must be controlled to 0.5 % or better. This is required over the whole dynamic

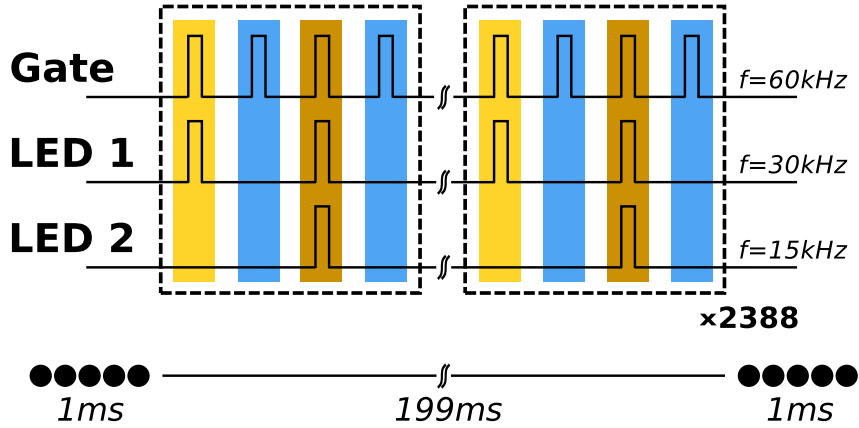


**Figure 17:** Possible trigger scheme for DNL measurements at the ILC. Between two bunch trains 2985 measurements of pedestal (blue), base light pulse (yellow), and base+differential (orange) pulse could be performed. This scheme allows for operating each LED with a constant frequency between the bunch trains. During a traversing bunch train both LEDs must not trigger.

range of the measurement, which stretches over an order of magnitude in the number of Compton scattered electrons per detector channel. The most populated channel has an average count rate of 100 – 200 electrons per bunch crossing, depending on the achieved laser-electron luminosity.

At the level of 0.5 %, a calibration via an external absolute reference light source is not trivial. The problem of calibrating the linearity of the light source can be circumvented by measuring directly the differential nonlinearity with two short (few ns) light pulses: The first pulse must be tunable to cover the whole dynamic range, but no special precision or linearity is required. The second pulse has a fixed size small compared to the maximal size of the base pulse. Again, its exact size does not need to be known, but it must be very stable, with not more than 0.5 % relative drift during a calibration cycle. The differential nonlinearity can then be measured from the response of the detector to the base pulse alone and to both pulses together. In case of the application at the ILC polarimeters, about 10 scan points for the base pulse with  $3 \times 10^6$  samples each are sufficient in order to achieve the required precision.

An LED driver providing these pulses has been designed and tested successfully in a setup using one of the candidate PMTs to be employed in the gas Cherenkov detectors of the ILC Compton polarimeters. In this setup, a correction of the nonlinearities to the per-mille level could be achieved. Transferring the result to a simulated polarisation measurement shows a negligible impact of the nonlinearity on the polarisation measurement after the correction. Finally, we propose a scheme how to collect calibration data in-situ during the physics runs of the ILC, exploiting the rather long gaps of 199 ms between the ILC bunch trains. A full calibration would then be completed within 1.5 hours, while more frequent updates of the calibration can be obtained by a sliding window technique.

In summary, the performance of the presented calibration system is sufficient to control the contribution of detector nonlinearities to the total uncertainty of the polarisation measurement to much better than 0.1 %. This could reduce the total systematic uncertainty

of the polarimeter measurements to  $\delta\mathcal{P}/\mathcal{P} = 0.2\%$ . In the future, the calibration system should be tested with the full prototype gas Cherenkov detector.

## Acknowledgement

The implementation and tests of the LED driver would not have been possible without the great technical support by Mathias Reinecke and Bernd Beyer. We thank our DESY colleagues in the CALICE collaboration for fruitful discussions about LED calibration systems. The results presented here could not be achieved without the National Analysis Facility and we thank the NAF team for their continuous support. We thankfully acknowledge the support by the BMBF-Verbundforschung in the context of the project “Spin-Management polarisierter Leptonstrahlen an Beschleunigern” and the DFG by Li/1560-1.

## References

- [1] G. Moortgat-Pick *et al.*, “The role of polarized positrons and electrons in revealing fundamental interactions at the linear collider,” *Phys. Rept.* **460** (2008) 131 doi:10.1016/j.physrep.2007.12.003 [hep-ph/0507011].
- [2] ILC Technical Design Report, 2013, <http://www.linearcollider.org/ILC/Publications/Technical-Design-Report>  
Volume 1: “Executive Summary,” [arXiv:1306.6327v1 [physics.ins-det]],  
Volume 2: “Physics,” [arXiv:1306.6352v1 [physics.ins-det]],  
Volume 3.I: “Accelerator R&D,” [arXiv:1306.6353v1 [physics.acc-ph]],  
Volume 3.II: “Accelerator Baseline Design,” [arXiv:1306.6328v1 [physics.acc-ph]],  
Volume 4: “Detectors,” [arXiv:1306.6329v1 [physics.ins-det]].
- [3] S. Boogert *et al.*, “Polarimeters and Energy Spectrometers for the ILC Beam Delivery System,” *JINST* **4**, P10015 (2009), doi:10.1088/1748-0221/4/10/P10015.
- [4] M. Beckmann, J. List, A. Vauth, and B. Vormwald, “Spin Transport and Polarimetry in the Beam Delivery System of the International Linear Collider,” *JINST* **9** (2014) P07003, doi:10.1088/1748-0221/9/07/P07003 [arXiv:1405.2156 physics.acc-ph].
- [5] J. List [ILD and SiD Collaborations], “Beam Polarisation and Triple Gauge Couplings in  $e^+e^- \rightarrow W^+W^-$  at the ILC,” *PoS EPS-HEP* **2013** (2013) 233, [http://pos.sissa.it/archive/conferences/180/233/EPS-HEP%202013\\_233.pdf](http://pos.sissa.it/archive/conferences/180/233/EPS-HEP%202013_233.pdf).
- [6] I. Marchesini, “Triple Gauge Couplings and Polarization at the ILC and Leakage in a Highly Granular Calorimeter,” PhD Thesis, University of Hamburg, 2011 (DESY-THESIS-2011-044), <http://www-library.desy.de/cgi-bin/showprep.pl?desy-thesis-11-044>.
- [7] A. Rosca, “Measurement of the beam polarisation at the ILC using the WW annihilation data,” LC-REP-2013-009, <http://www-flc.desy.de/lcnotes/notes/LC-REP-2013-009.pdf>.
- [8] G. Wilson, “Beam polarization studies with single bosons,” presentation at LCWS12 (Arlington, 2012), <https://agenda.linearcollider.org/event/5468/session/13/contribution/294>.
- [9] C. Bartels, J. Ebert, A. Hartin, C. Helebrant, D. Kafer and J. List, “Design and Construction of a Cherenkov Detector for Compton Polarimetry at the ILC,” *JINST* **7** (2012) P01019 [arXiv:1011.6314 physics.ins-det].

- [10] M. L. Swartz, “A Complete order  $\alpha^3$  calculation of the cross-section for polarized Compton scattering,” *Phys. Rev. D* **58** (1998) 014010 [hep-ph/9711447].
- [11] K. Abe *et al.* [SLD Collaboration], “A High precision measurement of the left-right Z boson cross-section asymmetry,” *Phys. Rev. Lett.* **84** (2000) 5945 [hep-ex/0004026].
- [12] D. P. Barber *et al.*, “The HERA polarimeter and the first observation of electron spin polarization at HERA,” *Nucl. Instrum. Meth. A* **329** (1993) 79.
- [13] D. P. Barber *et al.*, “The First achievement of longitudinal spin polarization in a high-energy electron storage ring,” *Phys. Lett. B* **343** (1995) 436.
- [14] V. Gharibyan *et al.*, “The TESLA Compton Polarimeter,” LC-DET-2001-047, <http://www-flc.desy.de/lcnotes/LC-DET-2001-047.pdf>.
- [15] U. Fano, *J. Op. Soc. Am.* **39** (1949) 859.
- [16] I. Ben Mordechai and G. Alexander, “A Transverse Polarimeter for a Linear Collider of 250 GeV  $e^+e^-$  Beam Energy,” LC-M-2012-001 <http://www-flc.desy.de/lcnotes/LC-M-2012-001.pdf>.
- [17] M. Beckmann *et al.*, “The Longitudinal polarimeter at HERA,” *Nucl. Instrum. Meth. A* **479** (2002) 334 [physics/0009047].
- [18] K. Moffeit, “Downstream Extraction Line Polarimeter,” Proceedings of the Workshop on Polarization and Energy Measurements at the ILC, Zeuthen, April 2008, <https://indico.desy.de/getFile.py/access?contribId=11&sessionId=1&resId=0&materialId=paper&confId=585>.
- [19] K. Moffeit, T. Maruyama, Y. Nosochkov, A. Seryi, M. Woodley and M. Woods, “Proposal to Modify the Polarimeter Chicane in the ILC 14 mrad Extraction Line,” SLAC-PUB-12425.
- [20] J. List, A. Vauth and B. Vormwald, “A Quartz Cherenkov Detector for Compton-Polarimetry at Future  $e^+e^-$  Colliders,” *JINST* **10** (2015) 05, P05014, doi:10.1088/1748-0221/10/05/P05014 [arXiv:1502.06955 [physics.ins-det]].
- [21] K. O. Eyser, C. Helebrant, D. Käfer, J. List and U. Velte, “Simulation Studies and Detector Scenarios for an ILC Polarimeter,” [arXiv:0709.2859 physics.ins-det].
- [22] C. Helebrant, “In Search of New Phenomena using Polarization – HERA and ILC,” PhD Thesis, University of Hamburg, 2009 (DESY-THESIS-2009-049), <http://www-library.desy.de/cgi-bin/showprep.pl?desy-thesis-09-049>.
- [23] B. Vormwald, “From Neutrino Physics to Beam Polarisation – a High Precision Story at the ILC,” PhD Thesis, University of Hamburg, 2014 (DESY-THESIS-14-006), <http://www-library.desy.de/cgi-bin/showprep.pl?desy-thesis-14-006>.
- [24] M. Reinecke, “Towards a full scale prototype of the CALICE Tile hadron calorimeter,” *IEEE Nucl.Sci.Symp.Conf.Rec.* **2011**, 1171–1176 (2011).